RSC Advances

PAPER

View Article Online
View Journal | View Issue

Cite this: *RSC Adv.*, 2025, **15**, 40478

Optimization of microstructure in high-silver content conductive inks *via* solvent volatilization modulation for application in flexible electronics

Qisong Feng,[ab] Junjun Ma,[ab] Yankun Shen,[ab] Zheng Zhou,[ab] Shilian Wu,[ab] Juan Wang,[ab] Junpeng Li*[cde] and Yu Yang *[ab]

Flexible printed electronics represent a swift, efficient, and cost-effective technique for depositing metallic conductive materials onto flexible substrates, particularly with the pivotal advancement of functional conductive inks. Metal–organic decomposition conductive inks have garnered substantial interest owing to their straightforward synthesis, convenient storage, and low processing temperatures. However, during low-temperature heating, these inks frequently encounter issues such as fast pyrolysis and gas escape, leading to numerous defects in the microstructure of silver films. Moreover, low silver content results in a high volumetric shrinkage rate, negatively impacting electrical conductivity. To address these limitations, this study synthesized four distinct silver precursors and conducted an in-depth analysis of their chemical compositions, thermal behaviors, and microscopic morphologies. Conductive inks were developed with a high silver content using silver citrate as the silver source with gradient thermal volatilization and low-temperature reduction properties. The impact of solvents and complexing agents on the performance of ink formulations was then examined. Furthermore, the evolution of the inks' microstructure was investigated during thermal decomposition along with the influence of the microscopic morphology on electrical conductivity. Finally, the thermal decomposition mechanism was elucidated in detail. By introducing organic solvents with varying boiling points, the intensity of thermal decomposition was effectively reduced, thereby minimizing the appearance of surface defects such as bubble holes and sintering marks. This strategy significantly enhanced the density of the silver film, reduced its surface roughness, and improved its electrical conductivity.

Received 5th March 2025
Accepted 9th June 2025

DOI: 10.1039/d5ra01591j

rsc.li/rsc-advances

1 Introduction

Flexible printed electronics have demonstrated tremendous potential in the modern electronics industry due to their unique deformability, lightweight characteristics, and significant cost advantages.[1] They have also become a focal point of multidisciplinary research.[2–4] Compared to traditional methods for manufacturing electronic devices, such as photolithography, vacuum deposition, and chemical plating, flexible printed electronics utilize techniques such as screen printing and inkjet printing[5–7] to efficiently fabricate metalized patterns on flexible substrates, including thin films, paper, fabrics,[8] and rubber. This approach has been shown to reduce production costs whilst simultaneously improving efficiency.[9] Currently, this technology has been widely applied to the production of transparent and flexible components, including sensors,[10,11] electronic displays,[12,13] solar cells,[14] thin-film transistors,[15] and supercapacitors.[16–19]

In the domain of flexible printed electronics, the formulation of conductive inks is a critical issue, as it directly determines the print quality and electrical conductivity of the resultant films.[20–22] Silver is a common constituent in conductive ink formulations due to its excellent electrical conductivity and oxidation resistance.[23] Silver-based conductive inks can be classified into particle-based and particle-free inks.[24] Particle-based silver conductive inks consist of conductive microparticles, solvents, surfactants, and dispersants.[25] However, during storage, nanoscale silver particles have been observed to aggregate, resulting in nozzle clogging and compromising film uniformity and electrical conductivity.[26] Additionally, high-temperature sintering is required to achieve conductivity, which limits their application on flexible substrates. In contrast, particle-free conductive inks consist of specific silver precursor

[a]*Yunnan International Joint Research Center for Photoelectric Information Materials, School of Materials and Energy, Yunnan University, Kunming 650500, P. R. China. E-mail: yuyang@ynu.edu.cn*

[b]*International Joint Research Center for Optoelectronic and Energy Materials, School of Materials and Energy, Yunnan University, Kunming 650500, P. R. China*

[c]*State Key Laboratory of Advanced Technologies for Comprehensive Utilization of Platinum Metals, Kunming Institute of Precious Metals, Kunming, Yunnan 650106, China. E-mail: lijunpeng@ipm.com.cn*

[d]*Sino-Platinum Electronic Materials (Yunnan) Co., Ltd, Kunming, Yunnan 650503, China*

[e]*Sino-Platinum Metals Co., Ltd, Kunming, Yunnan 650106, China*

compounds, complexing agents, and solvents. These inks offer several advantages, including ease of synthesis, storage, and processing at low temperatures (<200 °C). Additionally, they exhibit a reduced risk of nozzle clogging. During low-temperature sintering, silver–ammonia complexes undergo reduction to metallic silver, which subsequently deposits on the substrate surface to achieve conductivity.[27–29] Consequently, these inks have become a focal point in research endeavors within the domain of flexible printed electronics.

At present, due to the sensitivity of flexible substrates to sintering temperatures, research on particle-free conductive inks is primarily focused on the development and design of silver precursors and the reduction of ink decomposition temperatures. Zhang *et al.*[30] employed silver oxalate as the silver source which enhanced the uniformity of silver nanoparticles in the films through the synergistic effect of short-chain and long-chain amines, reducing defects such as pores and cracks. Sintering at 170 °C for 20 minutes yielded a resistivity of 6.71 μΩ cm; nevertheless, the utilization of mixed amines resulted in ligand decomposition, thereby reducing the storage time of the ink. In contrast, Yang *et al.*[31] pioneered a multifaceted approach, utilizing a combination of silver malonate (AgMa) and silver oxalate (AgOx). This strategy enabled the reduction in decomposition temperature, enhancement of conductivity, and improvement in structural uniformity. However, sintering at 180 °C for 1 hour resulted in a resistivity of 20.88 μΩ cm. This is due to the high sintering temperature, which limits its application to more temperature-sensitive flexible substrates. In a subsequent study, Zhou *et al.*[32] used silver acetate as the precursor and, for the first time, applied 1-amino-2-propanol as the complexing agent. This approach resulted in a significant improvement in its binding capacity with silver ions compared to 2-aminoethanol. Utilizing a spray-coating method, silver films were formed on thermosensitive silk/epoxy composite substrates, achieving a conductivity greater than 10^5 S m^{-1} after sintering at 150 °C. Nevertheless, due to inherent temperature limitations, further optimization is required to meet the demands of industrial applications. Sun *et al.*[33] Utilized multiple silver sources to develop a pore-filling mechanism during decomposition at various temperatures, enhancing the density and conductivity of the silver films. The preparation of the silver films on PI substrates was accomplished through the Utilization of spin-coating, followed by sintering at 100 °C for a duration of 40 minutes. This process resulted in a resistivity of 16.8 μΩ cm. In a related study, Chen *et al.*[34] synthesized conductive ink using silver malonate, diethanolamine, and ethylene glycol. XRD and SEM analyses revealed a synergistic effect between pyrolysis and silver reduction, forming high-quality silver films with a face-centered cubic (FCC) crystal structure. The fabrication of the silver films was accomplished *via* screen printing on polyimide (PI) substrates. It was found that a heat treatment at 150 °C for one hour achieved a conductivity of 1×10^6 S m^{-1}. Jahn *et al.*[35] used silver nitrate as the silver source, triethylamine as the complexing agent, and 2-[2-(2-methoxyethoxy)ethoxy] acetic acid as the solvent. By employing inkjet printing and UV curing, silver films with a conductivity of 1.1×10^7 S m^{-1} were achieved on PET films. In addition, the interaction between the ink and the substrate directly affects the microscopic morphology and electrical conductivity of the sintered metal film, which is closely related to the organic decomposition ink composition. The molecular structure of the precursor silver determines the thermal decomposition temperature of the coordination complex. Dong *et al.*[36] used silver tartrate as the precursor for their study and found that when the ratio of silver content to silver amine is reduced, the sintered silver film will form larger line widths and pores. This study also emphasized that the thermal decomposition of the complexes needs to be matched with the simultaneous volatilization of the organic components, which is a key factor in the formation of dense films. The complexing agent has a significant effect on the solubility, thermal decomposition temperature, and sintering densification of the precursor, and the nitrogen atoms in different amine compounds form coordination complexes with silver with significantly different thermal decomposition temperatures and coordination modes.[33] When the thermal decomposition temperature is too low, the violent decomposition will lead to the rough surface structure of the silver film, while when the temperature is too high, the slow decomposition will cause organic impurities to remain. At the same time, the solvent plays a key role in regulating the dispersion, spreading, and low-temperature volatilization characteristics of the ink.[20] However, during low-temperature heating, conductive inks often encounter challenges such as intense thermal decomposition reactions and gas release, leading to a multitude of defects in the microstructure of silver films. Additionally, the low silver content results in a high volumetric shrinkage rate. These issues remain insufficiently studied and require further research.

Therefore, this study synthesized four silver precursors and conducted a detailed investigation of their chemical composition, thermal decomposition process, and phase structures. Utilizing silver citrate as the silver source and monohydrated ethylenediamine as the complexing agent, the solubility of silver citrate in organic solvents was enhanced, leading to a reduction in the amount of organic solvent required and, consequently, an increase in the amount of silver loaded into the ink. The evolution of the ink's microstructure during thermal decomposition and the influence of microscopic morphology on electrical conductivity were systematically studied, and the thermal decomposition process of the ink was described in detail. Furthermore, gradient-evaporating organic solvents were formulated to allow the ink to volatilize gradually during low-temperature sintering. This approach led to a substantial mitigation of the reaction intensity, a reduction in the surface roughness and the bubble pore size of the silver film, an improvement in the film's density, and an enhancement in its electrical conductivity.

2 Experimental section

2.1 Experimental materials

All chemical reagents used in this study were of analytical grade (AR) or higher purity and did not require further purification. Silver nitrate (98%, YunNan LiYan Technology Co., Ltd),

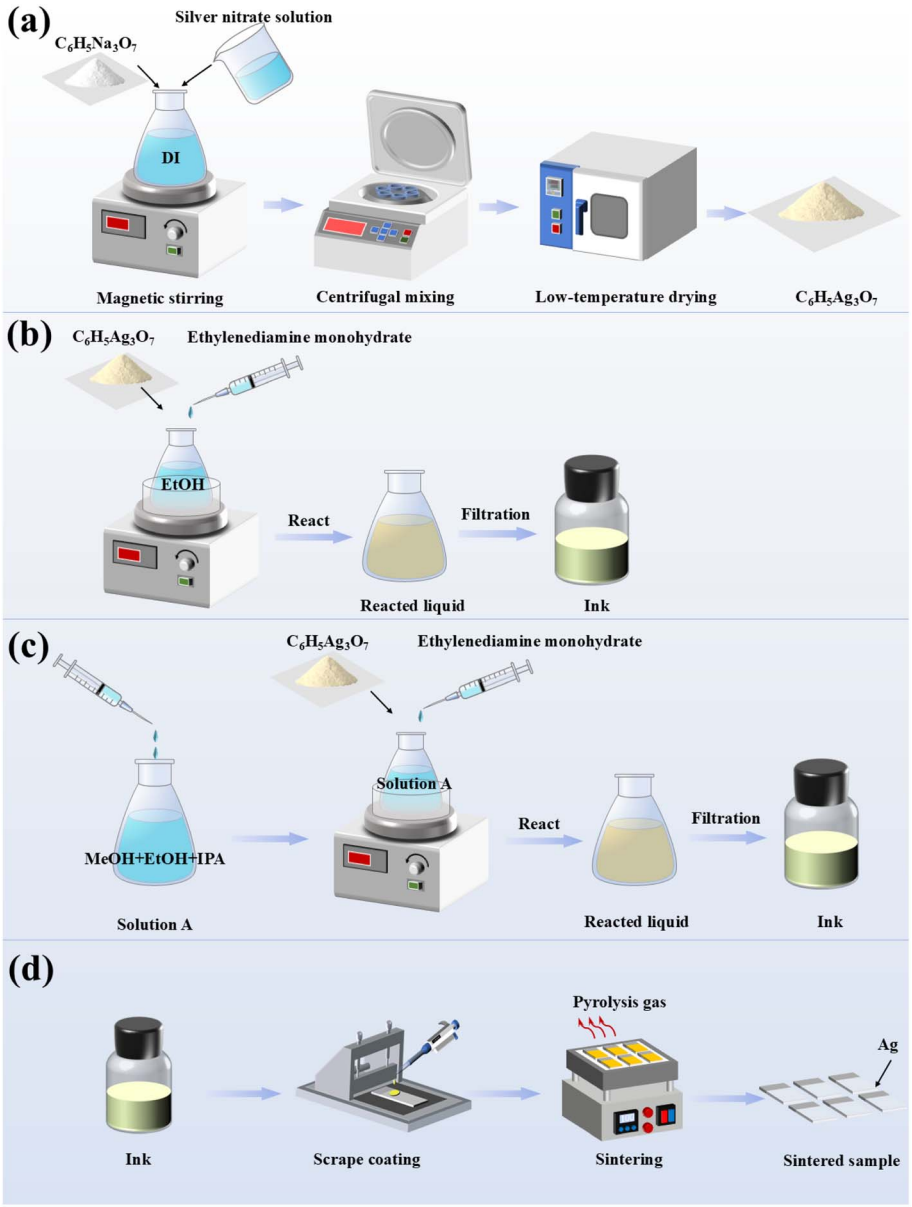

Fig. 1 (a) The synthesis process of silver citrate; (b) the preparation process of silver citrate conductive ink; (c) the improved preparation process of silver citrate conductive ink; (d) the deposition and sintering process of the ink.

sodium citrate (98%), sodium tartrate (98%), sodium oxalate (analytical grade, AR), anhydrous potassium carbonate (analytical grade, AR), methanol (98%), isopropanol (98%), ethanolamine (98%), ethylene glycol (98%), glycerol (99%), formic acid (99%), acetic acid (98%), phenolic resin (BR), polyvinylpyrrolidone (PVP), and monohydrated ethylenediamine (98%) were purchased from Shanghai Aladdin Biochemical Technology Co., Ltd. Ethanol was supplied by Tianjin Zhiyuan Chemical Reagent Co., Ltd PI, and PET substrates were provided by Zhongshan ChenXi Technology Co., Ltd; glass slides with specifications of 25 × 75 × 1 mm were supplied by Jiangsu Shitai Experimental Instrument Co., Ltd. The deionized water used in the experiments was prepared in the laboratory. Synthesis of silver precursors, formulation, and sintering of ink.

Fig. 1(a) illustrates the technical steps involved in the preparation of silver citrate powder. The detailed steps are as follows: Weigh 2.58 g of sodium citrate and dissolve it in 50 mL of deionized water. Stir for 10 minutes until fully dissolved, then add 30 mL of 1 mol L^{-1} silver nitrate solution. Continue stirring under light-protected conditions for 2 hours to form white silver citrate precipitates. The resulting precipitate was washed with deionized water by centrifugation at 8000 rpm for 5 minutes, repeated 3 times, and then washed once with anhydrous ethanol. Subsequently, the precipitate was dried in an oven at 40 °C for 10 hours. After drying, it was ground and passed through a 100-mesh sieve to obtain light yellow silver citrate powder (see Fig. S1 for the synthesis steps and reaction equations of silver tartrate, silver oxalate, and silver carbonate). The reaction equation is as follows:

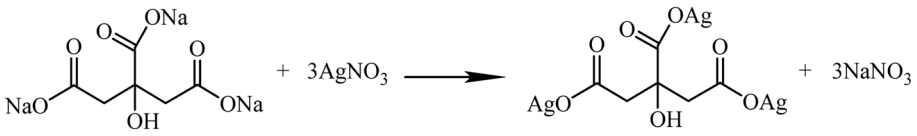

Fig. 1(b) illustrates the preparation process of the conductive ink. Weight 0.5126 g of synthesized silver citrate powder and add it to 1 mL of ethanol. Stir for 10 minutes to ensure it is fully mixed and uniform. Then, slowly add 0.4 mL of monohydrated ethylenediamine dropwise, followed by 0.005 g of PVP and 0.005 g of phenolic resin. Continue stirring under light-protected and ice-bath conditions for 30 minutes until no visible particles remain in the liquid. The resulting particle-free solution is filtered using a 0.22 μm filter to obtain a transparent conductive ink. The prepared ink should be stored at a low temperature of 5–10 °C for future use. The synthesis reaction equation is as follows:

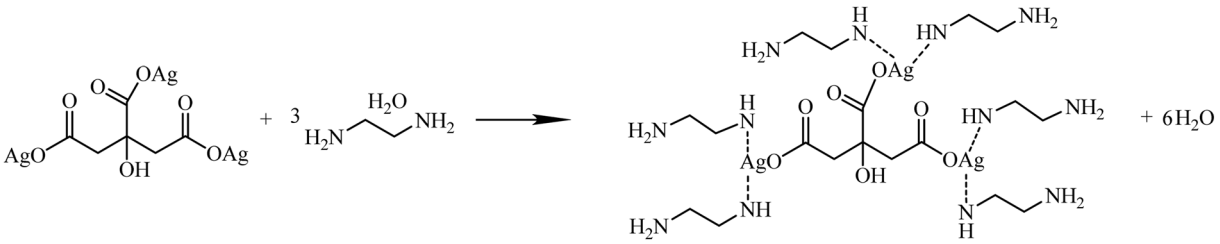

Fig. 1(c) illustrates the preparation process of the improved conductive ink. Equal volumes of methanol, ethanol, and isopropanol were mixed uniformly to prepare solution A. Then, 0.5126 g of silver citrate was weighed and added to 1 mL of solution A. Stir until a uniform solution (solution B) was obtained. Next, 0.4 mL of monohydrated ethylenediamine was slowly added dropwise to solution B, followed by the addition of 0.005 g of PVP and 0.005 g of phenolic resin. Stirring continued under light-protected and ice-bath conditions for 30 minutes until no visible particles remained in the liquid. The resulting solution was filtered using a 0.22 μm filter to obtain the transparent improved ink. The improved ink should be stored at a low temperature of 5–10 °C for future use.

To ensure the ink's good spreadability and printability on flexible substrates, PET, PI, and glass slides were treated with UV-ozone in the experiment. The synergistic effect of UV light and ozone can deeply clean the substrate surface, remove organic substances, and significantly improve the hydrophilicity of the material. After treatment, ink was dropped onto different substrates, and the contact angles were measured to evaluate wettability (see Fig. S2). Fig. 1(d) illustrates the process of blade-coating and thermal sintering of ink on a glass slide. The procedure is as follows: first, place the slide on a slide rack and ultrasonically clean it with ethanol solution and deionized water for 5 minutes, then dry it in an oven at 40 °C and wash it with a UV washer for 20 minutes to ensure that the surface is clean, and then set it aside for use. The cleaned slides were placed on the scratch pad substrates, and the appropriate amount of ink was accurately pipetted onto the slides using a pipette gun. Then, adjust the scraper to a fixed height and scrape the ink evenly at a certain speed to cover the entire surface of the slide. After scraping, the slide was carefully picked up with tweezers and placed on a sintering stage for thermal sintering at a set temperature.

2.2 Characterization

The sheet resistance of silver films was measured using a four-point probe tester (FT-330) to evaluate electrical conductivity. Fourier-transform infrared spectroscopy (Nicolet iS10) analyzed functional group structures in silver precursors and inks. A simultaneous thermal analyzer (STA449F3) examined the thermal decomposition of silver precursor powders and inks. Scanning electron microscopy (Quanta-200) and field emission scanning electron microscopy (Nova NanoSEM 450) assessed the morphology, structural uniformity, and density of sintered silver films. Metallographic microscopy (E1-G) characterized macroscopic uniformity, while atomic force microscopy (Bruker MultiMode 8) quantified three-dimensional surface morphology and roughness. X-ray diffraction (SmartLab SE) determined the crystalline structure of silver precursors, inks,

and films. UV-visible spectrometry (Lambda 650S) evaluated ink transparency, and a contact angle tester (SDC-200S) measured ink spreading and wetting properties.

3 Results and discussion

3.1 Characterization of precursor silver

The selection of silver precursors is critical for determining the sintering temperature and electrical performance of conductive inks, as they serve as the metallic source. Although various silver precursors have been synthesized in prior studies, their thermal decomposition mechanisms remain insufficiently elucidated. In this study, EDS, XRD, DSC-TG, and scanning electron microscopy were used to analyze the morphology, elemental composition, crystal structure, and thermal decomposition behavior of synthesized silver precursors to select the appropriate precursor.

Fig. 2(a–d) shows the Fourier-transform infrared spectra (FTIR) of four synthesized silver precursors. For silver carboxylates, the hydroxyl characteristic peaks are in the 3000–3750 cm^{-1} range, the asymmetric stretching vibration of carboxylate carbonyls appears at 1650–1550 cm^{-1}, and the symmetric stretching vibration is at 1440–1350 cm^{-1}. These characteristic peaks are observed in Fig. 2(a–c), indicating that these samples have carboxylate structures. For instance, the FTIR spectrum of silver citrate as an example (Fig. 2(a)), the absorption peak at 3338.4 cm^{-1} corresponds to the O–H hydroxyl group, 1589.4 cm^{-1} to the asymmetric stretching vibration of the C=O carbonyl, and 1396.8 cm^{-1} to its symmetric stretching vibration, while 1322.9 cm^{-1} corresponds to the stretching vibration of the C–O bond in carboxylates. Furthermore, the sharp peaks at 912.2 cm^{-1} and 848.6 cm^{-1} are caused by the bending vibrations of the Ag–O groups.[31] Fig. 2(d) shows the FTIR spectrum of silver carbonate. The peak at 1634.4 cm^{-1} corresponds to the asymmetric stretching vibration of the C=O group, while the peak at 1380.4 cm^{-1} corresponds to its symmetric stretching vibration, both of which are characteristic absorption peaks of carbonates. Additionally, the peaks at 881.3 cm^{-1} and 705.2 cm^{-1} correspond to the out-of-plane bending vibration of the C–O group and the bending vibration of the O–C–O group, respectively, indicating a carbonate structure.

The thermal decomposition behavior was analyzed using DSC-TG. Fig. 2(e–h) shows the DSC-TG curves of the four synthesized silver precursors. Fig. 2(e) shows the thermogravimetric analysis (DSC-TG) curve of silver citrate. Thermal decomposition mainly occurs between 156 °C and 200 °C, with rapid decomposition peaking at 175 °C, accompanied by a significant endothermic peak. This process is attributed to the thermal decomposition of silver citrate into silver aconitate or itaconate, which further decomposes into metallic silver. According to Robert *et al.*,[37] the first stage of citric acid's thermal decomposition involves intramolecular dehydration, followed by the formation of intermediate aconitic acid or itaconic acid,

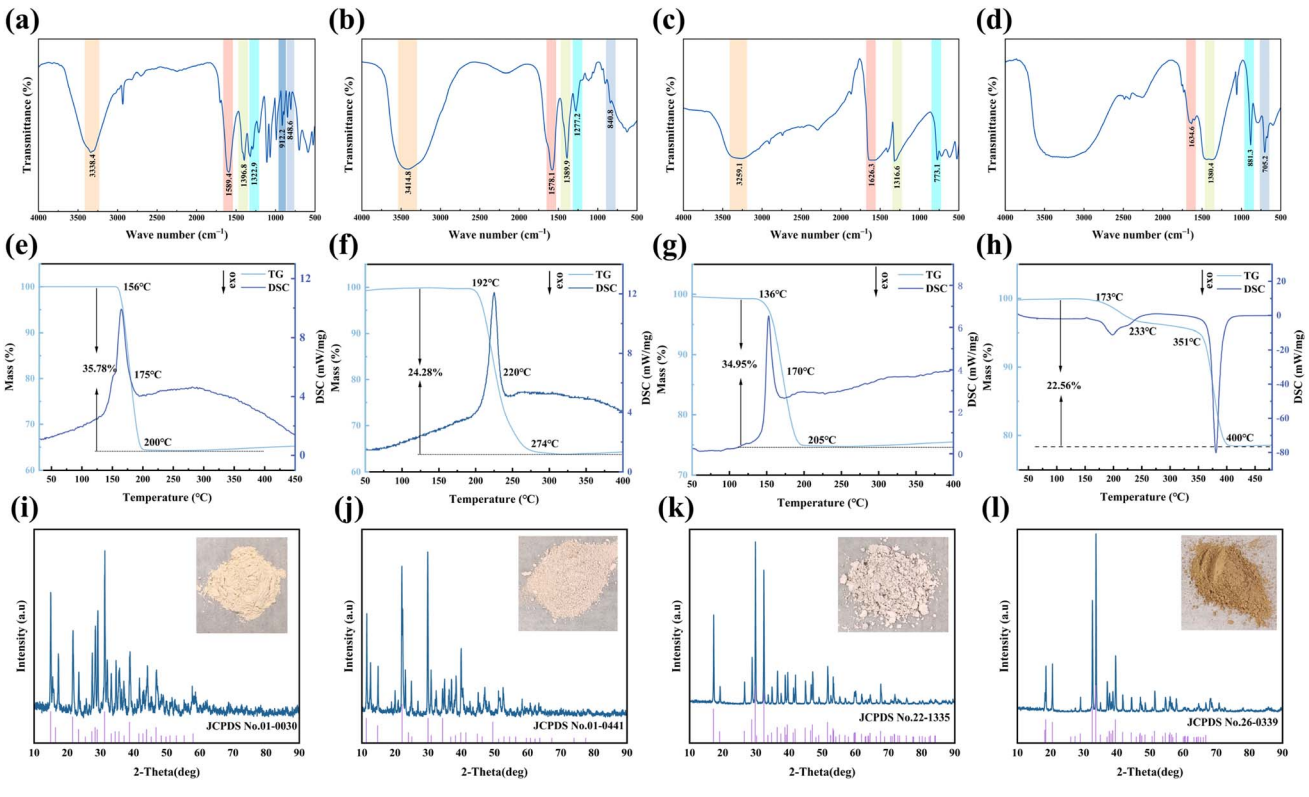

Fig. 2 Characterization of synthesized silver precursors: (a–d) Fourier-transform infrared spectra (FTIR) of silver citrate, silver tartrate, silver oxalate, and silver carbonate; (e–h) DSC-TG curves of silver citrate, silver tartrate, silver oxalate, and silver carbonate; (i–l) XRD patterns of silver citrate, silver tartrate, silver oxalate, and silver carbonate.

Table 1 Theoretical and actual silver content of precursors

Sample	Theoretical silver content (%)	Determination of silver content (%)
Silver citrate	63.2	65.4
Silver tartrate	59.3	65.05
Silver oxalate	71.1	75.72
Silver carbonate	78.3	78.6

which further converts into anhydride. Fig. 2(f) shows the thermogravimetric analysis (DSC-TG) curve of silver tartrate. The initial thermal decomposition of silver tartrate occurs around 192 °C, releasing water and carbon dioxide. A strong exothermic peak appears between 192 °C and 220 °C, corresponding to the complete decomposition of organic components and the formation of silver oxide. Subsequently, at higher temperatures, silver oxide further decomposes into metallic silver and oxygen. Fig. 2(g) shows the DSC-TG curve of silver oxalate. The thermal decomposition of silver oxalate occurs between 130 °C and 200 °C, with the peak centered at 170 °C. No phase transitions occur within this temperature range; the primary decomposition mechanism involves the cleavage of the C–C bond in oxalate ions, directly forming Ag and CO_2.[38] Fig. 2(h) shows that the thermal decomposition of silver carbonate involves two stages. The first stage occurs between 173 °C and 233 °C, where silver carbonate decomposes into silver oxide. The second stage of thermal decomposition occurs between 251 °C and 400 °C, where silver oxide decomposes into Ag and O_2.[39] Table 1 compares the theoretical and experimentally measured silver content of the precursors. The results show that the experimentally measured silver content is generally higher than the theoretical value, which may be attributed to the presence of trace residual impurity elements after sintering.

The microstructure and elemental composition of the synthesized silver precursors were analyzed using scanning electron microscopy (SEM) and energy-dispersive X-ray spectroscopy (EDS). As shown in Fig. S3, aside from the platinum coating, the precursors were composed primarily of C, O, and Ag. SEM images revealed distinct microstructural features: silver citrate exhibited irregular aggregates with densely distributed particles; silver tartrate displayed a flake-like structure with clear crystalline boundaries; silver oxalate featured needle-shaped crystals with uniform alignment, reflecting pronounced crystallinity; and silver carbonate showed blocky, granular morphology with smooth surfaces, indicative of stable crystal growth. These structural characteristics aligned with their respective thermal decomposition behaviors observed in DSC analysis.

Fig. 2(i–l) presents the X-ray diffraction (XRD) spectra of the four silver precursors. For silver citrate, the diffraction peaks at 11.48°, 14.92°, 22.14°, 29.82°, and 39.96° matched the standard pattern (JCPDS No. 01-0030), and the combination of the above FIRTs and EDS proves that it is a target substance. Similarly, the XRD spectra of silver tartrate, oxalate, and carbonate in Fig. 2(j–l) aligned with their respective standard diffraction patterns, verifying the structural integrity and purity of the synthesized materials. Laboratory-synthesized samples (Fig. 2(i–l)) also exhibited colors and appearances consistent with standard ref. 40–43, further supporting their reliability as target compounds.

Among the four precursor species, silver citrate has a lower thermal decomposition temperature and is more storage stable. After preliminary experiments, the complexation reaction of silver citrate was rapid, and the synthesis was stable. Therefore, silver citrate was chosen as the main research object.

3.2 Synthesis and characterization of primitive ink

The composition of particle-free conductive ink were systematically investigated with a focus on solvents and complexing agents. The wettability of the ink on the substrate is one of the key factors affecting its performance in the study of the preparation and application of organic decomposition conductive inks. The wettability determines the spreading ability of the ink on the substrate, which in turn affects the film-forming quality of the ink as well as the final conductive properties. Among them, the performance of solvents plays a crucial role in the wettability of inks. Therefore, this study experimentally compares the wettability of different solvents on different substrates in order to provide a theoretical basis for the optimization of the formulation of organic decomposition conductive inks. As shown in Table 2, the experimental results show that among the five solvents tested, the contact angles of methanol, ethanol, and isopropanol on the substrate are relatively small, and the specific test results are shown in Fig. S5. The smaller contact angles mean that the solvents have a better spreading ability on the substrate, and they can be distributed more uniformly on the surface of the substrate, which can provide favorable conditions for the good film formation of the conductive ink. Therefore, these three solvents are more suitable for flexible substrates such as PET and PI films. Further, experiments compared the solubility of silver citrate in different solvents and its complexation ability with various complexing agents (summarized in Table S1). The results showed that ethanolamine reacts with silver citrate to form a complex, turning the solution dark brown. Due to their high viscosity, ethylene glycol and propylene glycerol were unsuitable as solvents because they could not fully dissolve or disperse silver citrate. In contrast, methanol, ethanol, and isopropanol effectively dispersed silver citrate, with ethanol being the most suitable due to its solubility and spreadability.

Table 2 Contact angle size of different solvents on different substrates

Solvent	Glass (CA°)	PET (CA°)	PI (CA°)
Methanol	7.006	7.880	13.788
Ethanol	5.525	7.827	12.529
Isopropanol	6.789	8.984	11.709
Ethanolamine	10.305	37.711	28.354
Ethylene glycol	11.536	49.225	54.554
Glycerine	22.780	66.373	99.926

Table S2 summarizes the reactions between silver citrate and various complexing agents. Ethanamine and monohydrated ethylenediamine rapidly completed complexation, while *n*-propylamine and isobutylamine formed complexes more slowly due to spatial potential resistance from longer carbon chains, which reduced nitrogen reactivity. Diamines demonstrated stronger complexation ability than monoamines due to their multi-coordination properties, enhancing silver citrate dispersion and promoting bound water desorption, thereby increasing silver content in the ink. Thereforce, monohydrated ethylenediamine was identified as the preferred complexing agent for silver citrate. Fig. S6(a) shows the reaction results under different silver-to-amine molar ratios. As the silver-to-amine ratio gradually increases from 1 : 1 to 1 : 6 (see formulations in Table S3), the system transitions from dispersion to complete complexation, forming a deep black homogeneous solution. Fig. S6(b) displays the filtered ink images. When the silver-to-amine ratio reaches 1 : 3, the complexation reaction of silver citrate is nearly complete, resulting in an orange-yellow ink. When the ratio is further increased to 1 : 4 or higher, the transparency of the system increases, likely due to the residual excess of monohydrated ethylenediamine. Therefore, the solubility of silver citrate is optimal at a silver-to-amine ratio of 1 : 3.

The stability of conductive ink is essential for its printing performance and electrical conductivity. Silver nanoparticles typically exhibit surface plasmon resonance (SPR) transitions, generating characteristic absorption peaks in the visible light range of 380–450 nm, and appear yellowish-brown.[44–46] However, as shown in Fig. 3(a), the UV-visible absorption spectrum of the ink lacks these characteristic peaks. The ink appears as a yellow-orange transparent liquid, indicating the absence of residual silver citrate or decomposed silver–amine complexes, thereby confirming its excellent storage stability. The complexation process was confirmed using Fourier-transform infrared (FTIR) spectroscopy. Fig. 3(b) presents the FTIR spectra of monohydrated ethylenediamine and the reacted ink. Monohydrated ethylenediamine exhibits a broad O–H absorption peak at 3200–3600 cm^{-1}, an N–H absorption peak at 3349 cm^{-1}, and C–H peaks at 2947 cm^{-1} and 2877 cm^{-1}. In the ink spectrum, the N–H peaks redshifted to 3309 cm^{-1} and 3257 cm^{-1}, while the C–H peaks shifted slightly to 2943 cm^{-1} and 2871 cm^{-1}. The redshift of N–H indicates the formation of coordination complexes between the amino groups and silver ions, attributed to the interaction of the lone electron pairs on amino groups with the vacant orbitals of silver ions. In contrast, the C–H groups showed negligible changes. The thermal decomposition behavior of the ink was analyzed using DSC-TG. Fig. 3(c) presents the thermogravimetric analysis results, showing an initial mass loss around 79 °C due to solvent evaporation, followed by major thermal decomposition between

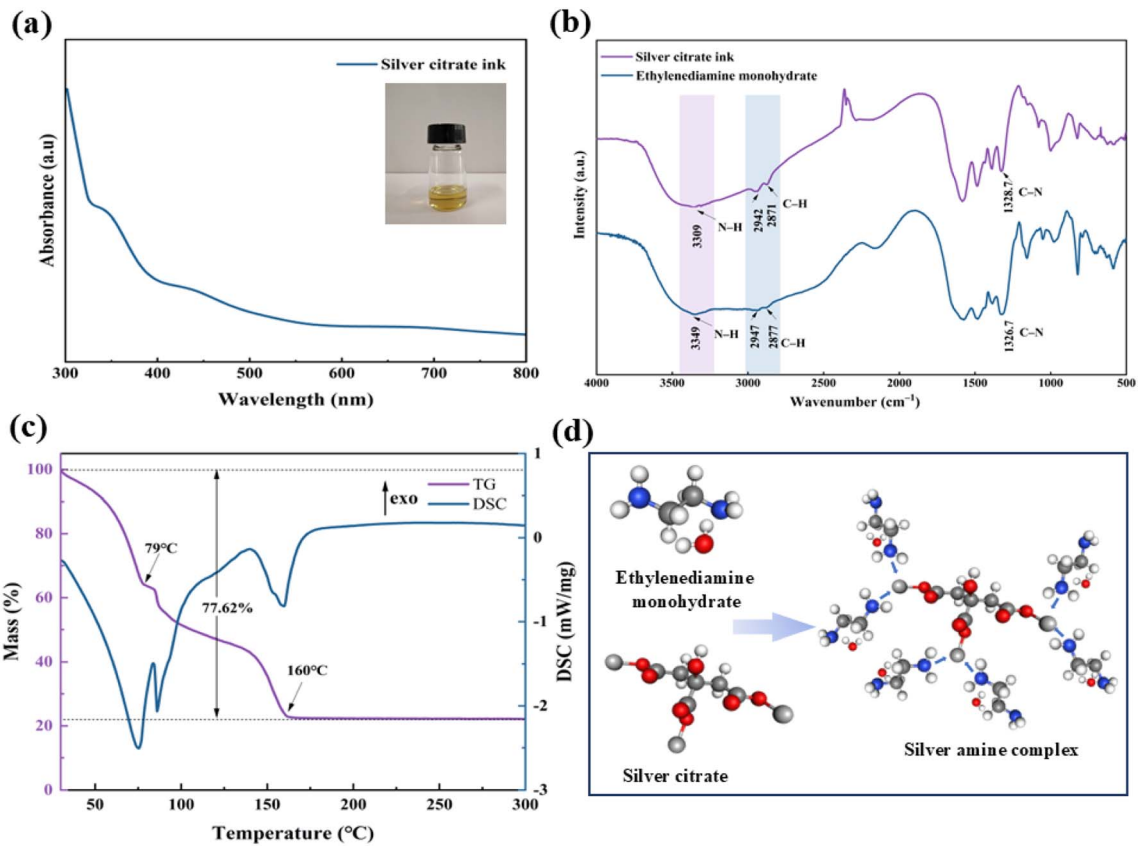

Fig. 3 Characterization and reaction diagram of silver citrate ink: (a) UV absorption spectrum of the ink; (b) Fourier-transform infrared (FTIR) spectra of the ink and monohydrated ethylenediamine; (c) thermogravimetric (TG) curve of the ink; (d) coordination process of monohydrated ethylenediamine with silver citrate.

130 °C and 160 °C. The decomposition rate increases significantly after 130 °C. Notably, the ink's decomposition temperature is lower than the initial decomposition temperature of silver citrate (156 °C, see Fig. 2(c)), confirming the successful formation of coordination complexes between monohydrated ethylenediamine and silver citrate. Fig. 3(d) illustrates the proposed coordination mechanism of silver citrate with monohydrated ethylenediamine.

3.3 Morphological characterization of sintered films from primitive ink

The thermal sintering process of organic conductive ink directly affects the conductivity of the silver film. Fig. S7 shows the square resistance value of the conductive ink at different heating rates in 140 °C sintering after holding 10 min. It can be found when the heating rate is 5 °C min^{-1} when the square resistance value is larger, while at 10 °C min^{-1} and 20 °C min^{-1} heating rates, the resistance value does not change much. This is because the organic conductive ink, to reach a certain temperature, began to thermally decompose and reduce to silver atoms. In the lower rate of heating, the thermal decomposition rate of the ink is slow, and the formation of the upper layer of silver particles prevents the internal thermal decomposition of impurities from escaping, so that the conductivity of the lower layer and the rate of heating to reach a certain condition of the conductivity of the ink have less impact. Fig. 4(i) shows a schematic diagram of the sintering and film-forming process of the ink spread on a glass slide. Fig. 4(a–d) presents low-magnification SEM images of silver films formed after sintering the conductive ink at 150 °C, 160 °C, 170 °C, and 180 °C for 10 minutes. The images reveal small pores and sintering marks on the surface of the silver film, distributed in a blocky manner. This is caused by the evaporation of organic solvents and ammonia gas during the thermal sintering of the ink. As the temperature further increases, the silver–amine complexes decompose thermally into silver atoms. The bubbles gradually escape from the interior and burst on the surface, resulting in the formation of sintering marks. The silver nanocluster sizes in the sintering mark areas are smaller compared to the surrounding regions. Fig. 4(e–h) shows SEM images of the ink sintered at 160 °C for different durations, revealing the evolution of the microstructure of the silver film. At 10 minutes of sintering (Fig. 4(e)), the silver atoms have just completed thermal decomposition and reduction, forming small nanoclusters with visible cracks and bubble pores between the clusters, mainly caused by the evaporation of organic solvents and thermal decomposition. At 20 minutes of sintering (Fig. 4(f)), the silver nanoclusters gradually connect, and some regions form larger silver microclusters, which are closely related to grain boundary movement and sintering neck formation. With extended sintering times of 40 and 60 minutes (Fig. 4(g and h)), the silver film surface is gradually covered by a large area of silver nanoclusters, whose sizes increase while cracks narrow. This indicates a denser structure and significantly improved conductive pathways. However, some loose areas remain in the silver film, which may have a certain impact on electron transport.

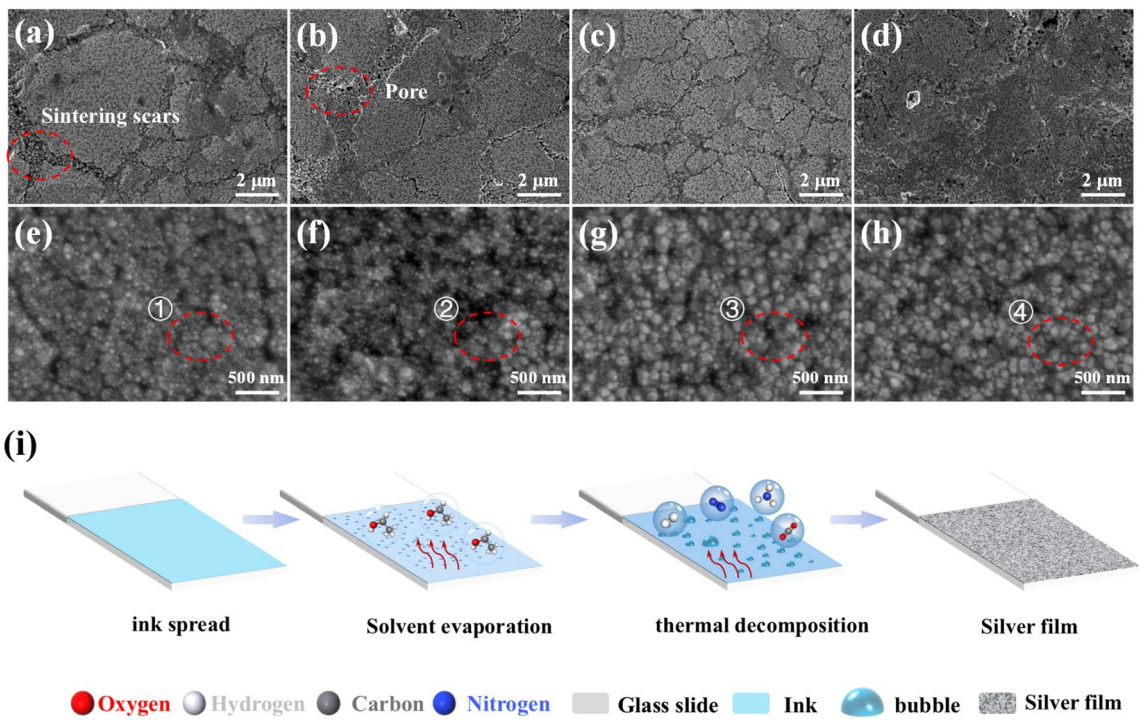

Fig. 4 SEM Images and sintering process diagram of the ink: (a–d) SEM images of the ink blade-coated on glass slides and sintered at 150 °C, 160 °C, 170 °C, and 180 °C for 10 minutes; (e–h) SEM images of the ink blade-coated on glass slides and sintered at 160 °C for 10 minutes, 20 minutes, 30 minutes, and 40 minutes; (i) schematic diagram of the sintering process of the silver film at 160 °C for different sintering durations.

3.4 Low-temperature sintering performance and microstructural characterization of improved ink

The rapid evaporation of the solvent and the intense thermal decomposition of the ink lead to numerous sintering marks and bubble pores on the surface of the silver film. Therefore, selecting solvents with different boiling points that evaporate at different temperatures is expected to reduce the size of bubble pores and the intensity of the reactions. This mechanism helps to form dense conductive pathways, improves the compactness of the silver film, and ultimately enhances its conductivity. Fig. 5 shows the metallographic morphology and atomic force microscopy (AFM) surface morphology analysis of silver films formed from inks with different composite solvents after sintering (formulations are listed in Table S4). The metallographic images show that the silver films retain some organic impurities and have bubbles of varying sizes on the surface caused by gas evaporation. These impurities and bubbles directly affect the conductivity of the silver film. Fig. 5(a–l, d–l, g–l and j–l) shows the bubble pore size distribution of silver films formed from inks with different composite solvents after sintering. For formulation A (single solvent), the bubble pore sizes mainly

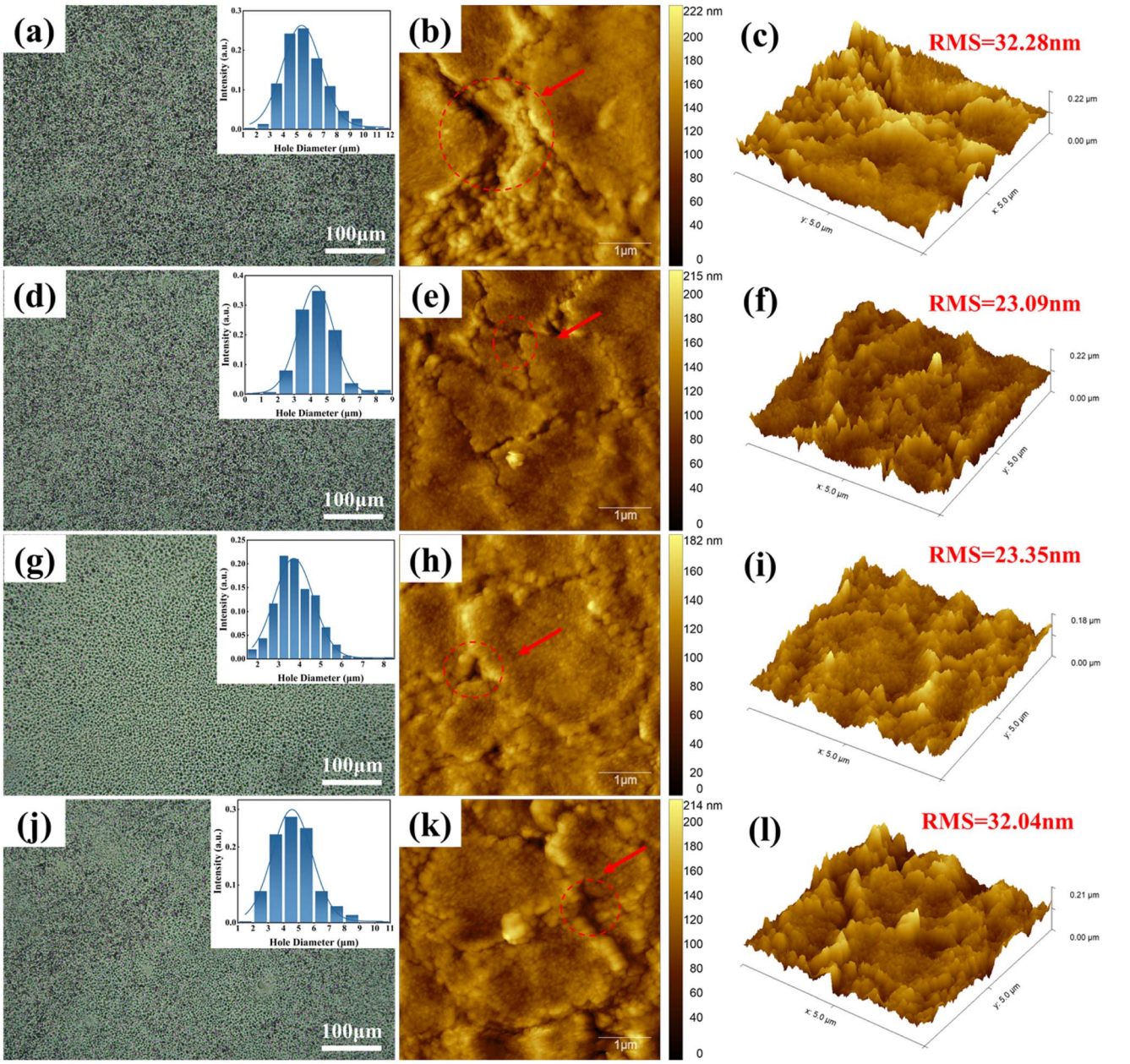

Fig. 5 (a, d, g and j) Correspond to the metallographic images of the films formed after sintering of the conductive inks in schemes A, C, D, and E in Table S4 at 500× magnification, respectively; (b, e, h and k) correspond to the AFM 2D images of the films formed after sintering of the conductive inks of schemes A, C, D, and E in Table S4, respectively; (c, f, i and l) correspond to the AFM 3D images of the films formed after sintering of the conductive inks of schemes A, C, D, and E in Table S4, respectively.

range from 4–6 nm, while formulations C and D are concentrated at 4–5 nm and 3–4 nm, respectively. The results indicate that the gradient evaporating solvents in formulations C and D significantly reduced bubble pore sizes through stepwise evaporation, thereby reducing the intensity of thermal decomposition. The decline in conductivity observed in formula E can be attributed to the incorporation of a modest quantity of deionised water. Following the volatilisation of methanol, ethanol and isopropanol, the organic ink exhibits an inability to maintain a uniform spread, consequently leading to a reduction in the uniformity of the ink post-scraping and film formation. This, in turn, results in a decline in film quality. Fig. 5(b, e, h, k) and (c, f, i, l) respectively show the 2D and 3D morphology of the silver film surfaces. The 2D images reveal surface undulations with distinct cracks, where the silver nanoclusters within the cracks are larger in size, while the smooth regions form dense silver films. After sintering, formulation A shows distinct bubble marks on the surface, while formulations C, D, and E show progressively reduced bubble marks. The roughness (RMS) values of the 3D surface morphology measured by AFM further confirm these results: the RMS for formulation A is 32.28 nm, while those for formulations C and D are 23.09 nm and 23.35 nm, respectively. The gradient boiling point solvents significantly reduced the surface roughness of the silver film, resulting in a denser microstructure conducive to electron transport. This is consistent with the sheet resistance results from the four-point probe test, demonstrating the crucial role of composite gradient solvents in improving the conductivity of silver films.

The silver films sintered at 120 °C to 200 °C were analyzed using X-ray diffraction (XRD). Fig. 6(a) presents the XRD patterns of silver films formed from silver citrate conductive ink at different sintering temperatures. The main diffraction peaks, located at 38.11°, 44.29°, 64.44°, 77.39°, and 81.53°, correspond to the (111), (200), (220), (311), and (222) crystal planes of the face-centered cubic (FCC) structure of metallic silver. These peaks align with the standard XRD pattern (JCPDS No. 87-0597), confirming that the sintered silver films are primarily composed of high-purity metallic silver. The silver loading and sintering temperature of particle-free conductive inks play a crucial role in the conductivity of silver films. Fig. 6(b) shows the DSC-TG curves of the scheme D ink formulation (Table S4), revealing stepwise decomposition associated with the boiling points of composite solvents. Methanol, ethanol, and isopropanol evaporate near their respective boiling points at lower temperatures. After complete thermal decomposition, the remaining solid mass is 28.47 wt%, indicating a silver loading of approximately 24%. The elemental composition of the sintered silver films was confirmed by energy-dispersive spectroscopy (EDS), as shown in Fig. 6(c), identifying silver as the primary component. Fig. 6(d) shows the average sheet resistance values of inks with different composite solvents tested after sintering at 160 °C for 10 minutes. The sheet resistance values of formulations A to E are 0.63 Ω/□, 0.62 Ω/□, 0.55 Ω/□, 0.54 Ω/□, and 0.71 Ω/□, respectively. When deionized water is introduced in formulation E, the sheet resistance instead increases to 0.71 Ω/□. The high boiling point of deionized water causes slow evaporation, forming larger bubble pores, reducing the compactness of the

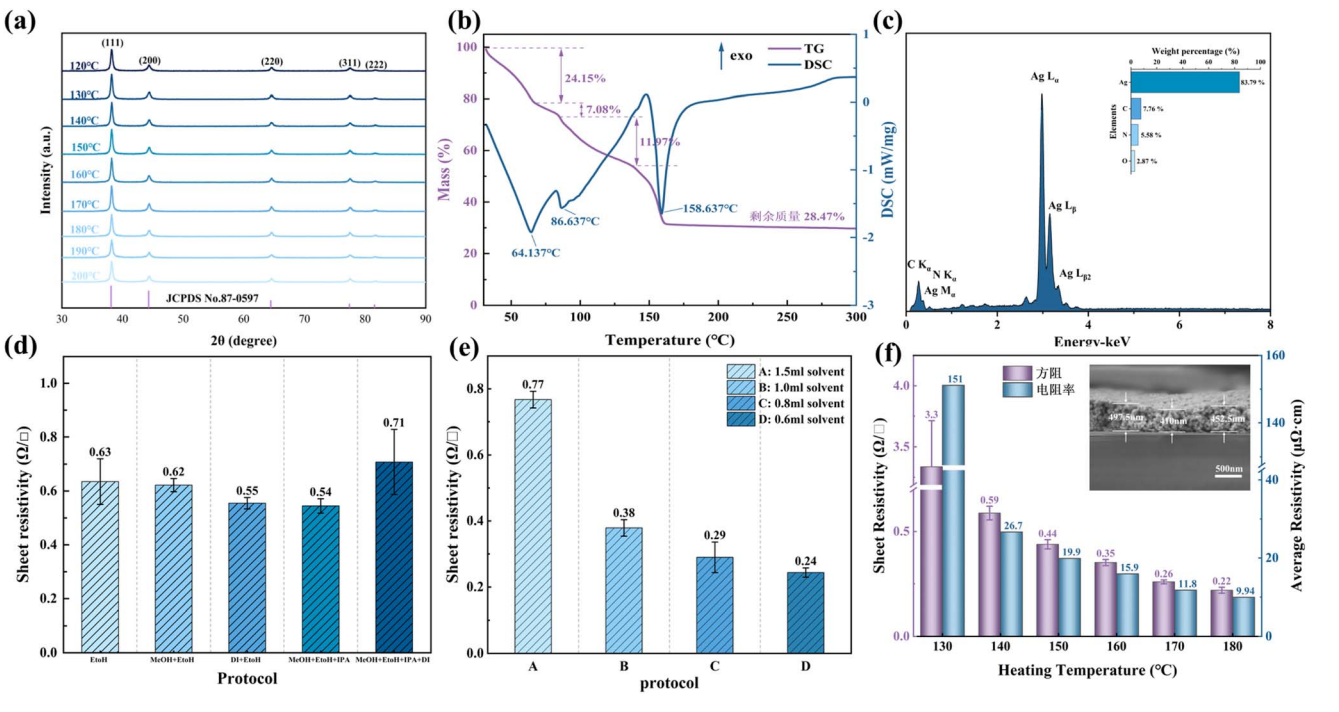

Fig. 6 (a) XRD patterns of conductive inks formed into films at different sintering temperatures; (b) thermogravimetric (TG) curve of the ink; (c) EDS of silver films sintered from the ink at 160 °C; (d) sheet resistance values of inks with different composite solvents sintered at 160 °C for 10 minutes; (e) sheet resistance values of inks with different silver contents sintered at 160 °C for 60 minutes; (f) electrical performance of inks sintered at different temperatures for 30 minutes and SEM cross-sections of the silver films.

silver film, and failing to improve conductivity. In contrast, formulations B to D use composite gradient solvents, significantly reducing the sheet resistance, with the lowest value reaching 0.54 Ω/□. This indicates that composite solvents effectively improve the conductivity of the silver film. Fig. 6(e) illustrates the sheet resistance of inks with varying silver contents sintered at 160 °C for 1 hour (formulations in Table S5). The results demonstrate that reducing the solvent amount and increasing the silver content significantly decrease the sheet resistance, thereby improving conductivity. Fig. 6(f) presents the sheet resistance and average resistivity of inks sintered at different temperatures. Fig. 6(f–l) demonstrates the average film thickness of the inked films to be 453 nm. High-silver-content inks sintered at 140 °C, 150 °C, 160 °C, 170 °C, and 180 °C for 30 minutes achieved resistivities of 26.7 μΩ cm, 19.9 μΩ cm, 15.9 μΩ cm, 11.8 μΩ cm, and 9.94 μΩ cm, respectively.

In order to further explore the application of organically decomposed conductive inks on flexible substrates, Fig. 7(a and b) shows the conductive properties of conductive inks after sintering in different atmospheres on PI and PET substrates. As in Fig. S9 (a_3 and b_3), the average thicknesses of silver films on PI and PET substrates are 545 nm and 695 nm, respectively. The lower conductivity of the inks after sintering on PET substrates compared to PI substrates is due to the fact that the softening temperature of PET is lower than that of PI films, and during the heating process, the deformation of PET films is greater after heating, which, on the one hand, makes the thermal decomposition of the silver film non-uniform and leads to a more sparse connection between the reduced silver nanoclusters (see Fig. S9). In addition, after sintering in inert gas, the conductivity of the silver film was better compared to direct sintering in air, which was attributed to the fact that some of the silver nanoparticles prevented from being oxidized during the reduction process in the inert atmosphere, and the surface elemental content of the silver film was tested after sintering in different atmospheres (see Fig. S10). Moreover, the resistivities were 29.5 μΩ cm, 15.6 μΩ cm, and 9.79 μΩ cm after sintering on PI substrates at 140 °C, 150 °C, and 160 °C for 30 min under inert gas, and the films were tested to achieve an adhesion grade of up to 5B by using the 100-gauge test method (see Fig. S11). Fig. 7(c) shows the silver conductive patterns and films sintered

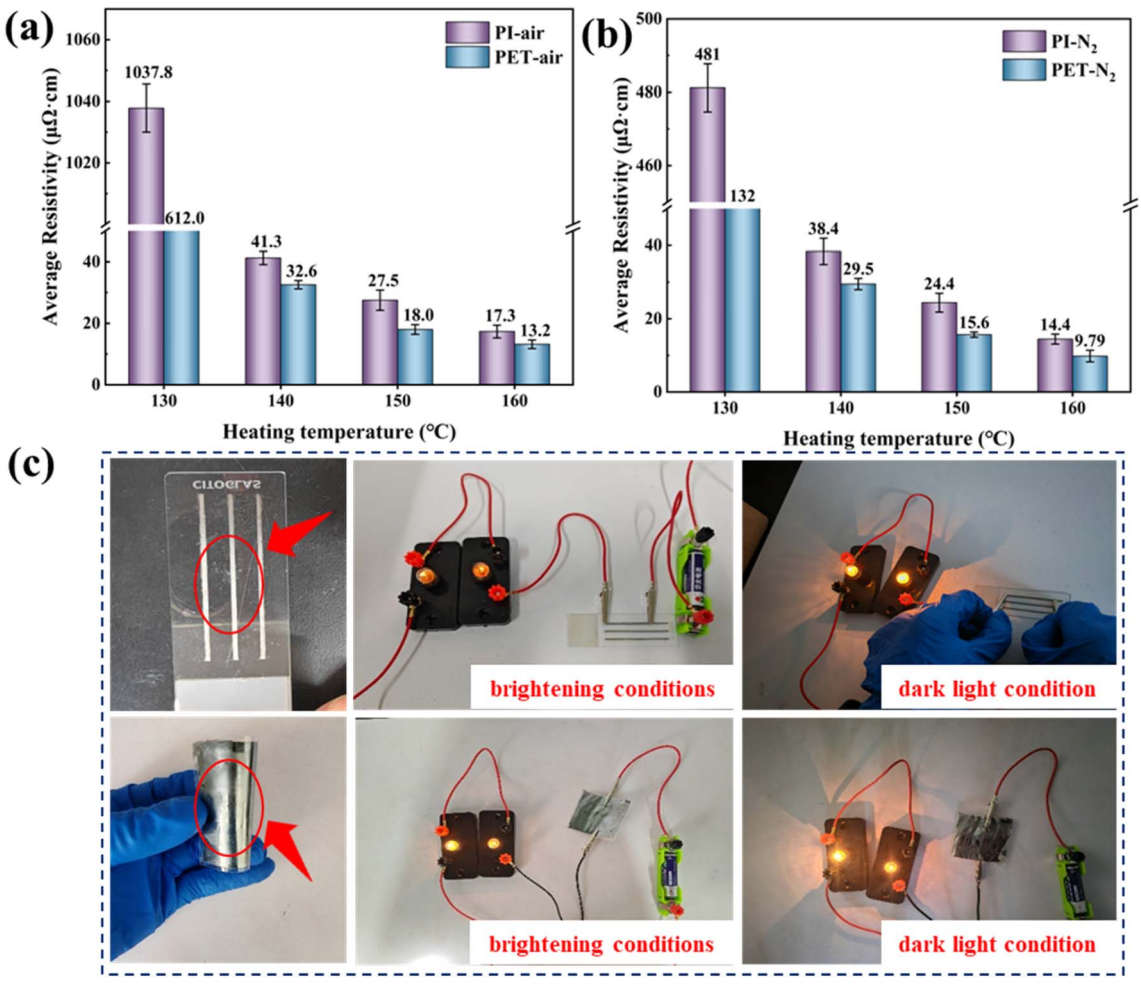

Fig. 7 (a) Organic decomposition inks sintered in air on PET and PI substrates; (b) organic decomposition inks sintered in nitrogen on PET and PI substrates; (c) photos of conductive ink coated on glass slides and PET films, and schematic of its application in conductive circuits.

on glass slides and PET films. The inks, after sintering at 150 °C for 30 min, showed a silvery-white metallic luster of pure silver, indicating that the formed silver films have high purity and metallic properties. In addition, experiments show that the prepared silver film has good flexibility and maintains excellent electrical conductivity even under simple bending. To verify the conductivity, two small 1.5 V light bulbs connected in series were successfully lit by connecting a No. 5 battery to the silver conductive line. This result shows that the prepared silver conductive inks have good potential for application in the field of flexible printed electronics and can meet the functional requirements of real circuits.

4 Conclusions

This study successfully synthesized four silver precursors, and the chemical composition, thermal behavior and physical phase structure of these precursors were also analyzed in detail. Among these precursors, silver citrate, which has the lowest thermal decomposition temperature (~175 °C) and excellent storage stability, was identified as the ideal precursor for conductive inks. A comprehensive investigation into the effects of solvents, complexing agents, and the molar ratio of silver to amine revealed that monohydrated ethylenediamine, through its multidentate coordination and dispersion effect following water desorption, facilitated the dissolution of silver citrate and increased the solid content in conductive inks to 28.47 wt%. It was determined that optimal ink performance was achieved at a molar ratio of 1 : 3 between silver and amine. Furthermore, the study elucidated the micro- and macro-scale evolution of particle-free conductive inks during thermal sintering, thereby clarifying the critical roles of solvent evaporation and nanoparticle clustering in forming dense silver films. A gradient solvent strategy, comprising methanol, ethanol, and isopropanol, was proposed, enabling stepwise solvent evaporation. This approach led to a substantial reduction in thermal decomposition intensity, minimized bubble pore sizes and cracks on the silver film surface, and enhanced the compactness and smoothness of the film. After being sintered in an inert gas atmosphere at a temperature of 150 °C for 30 minutes, the resistivity of the silver film was measured to be 15.6 μΩ cm. This study provides a theoretical and practical foundation for the development of flexible electronic devices and low-temperature printable conductive materials. The results of this study suggest that conductive ink silver has a wide range of potential applications in flexible electronics, wearable devices and low-temperature manufacturing processes.

Author contributions

Qisong Feng: writing – original draft, methodology, investigation, formal analysis, data curation, conceptualization. Junjun Ma: writing – review & editing, investigation, data curation. Yankun Shen: writing – review & editing, investigation, data curation. Zheng Zhou: writing – review & editing, investigation, data curation. Shilian Wu: writing – review & editing, methodology, investigation. Juan Wang: writing – review & editing, methodology, investigation. Junpeng Li: writing – review & editing, supervision, resources, project administration, funding acquisition, conceptualization. Yu Yang: writing – review & editing, supervision, resources, project administration, funding acquisition, conceptualization.

Conflicts of interest

The authors affirm that they possess no known competing financial interests or personal relationships that could have appeared to influence the findings presented in this paper.

Data availability

Data will be made available on request.

Supplementary information is available. See DOI: **https://doi.org/10.1039/d5ra01591j**.

Acknowledgements

We sincerely thank the funding support provided by the Department of Science and Technology of Yunnan Province 2025 Annual Basic Research Special-Major Program (No. 202501BC070004), the Fundamental Research Program of Yunnan Precious Metals Laboratory Co., Ltd (No. YPML-20240502007), and the Yunnan Province Xingdian Talent Program – Yunling Scholar Fund (No. KC194317). We also extend our gratitude to the Advanced Analysis and Measurement Center of Yunnan University for providing sample testing services.

References

1 J. Rao, B. He, F. Chen and J. Xia, *Transducer and Microsystem Technology*, 2023, **42**, 1–5.
2 J. Miao and T. Fan, *Carbon*, 2023, **202**, 495–527.
3 R. M. R. Pinto, S. S. Nemala, M. Faraji, A. Capasso and K. B. Vinayakumar, *Inkjet-Printing of Carbon Nano Onions for Sensor Applications in Flexible Printed*, IEEE, 2022, DOI: **10.1109/FLEPS53764.2022.9781548**.
4 J. X. Jiang, X. Chen, Z. X. Mei, H. T. Chen, J. Y. Chen, X. Wang, S. F. Li, R. Y. Zhang, G. F. Zheng and W. W. Li, *Micromachines*, 2024, **15**, 333.
5 S. Bi, B. H. Gao, X. Han, Z. R. He, J. Metts, C. M. Jiang and K. Asare-Yeboah, *Sci. China: Technol. Sci.*, 2024, **67**, 2363–2386.
6 T. Liu, J. Chen, J. Zhao, N. Chen, Y. Li, H. Liang, Y. Yang, R. Yao, H. Ning and J. Peng, *Mater. Rev.*, 2022, **36**(20), 21010127.
7 Y. Liu, H. Z. Zhu, L. Xing, Q. K. Bu, D. Y. Ren and B. Sun, *Nanoscale*, 2023, **15**, 6025–6051.
8 H. Wang, B. Wang, X. Ning, L. Qu and M. Tian, *J. Text. Res.*, 2021, **42**, 189–197.
9 S. H. Ke, Y. N. Liu, F. Chen, X. H. Ni and Y. X. Ma, *Polym. Adv. Technol.*, 2024, **35**, e6581.
10 Y. S. Rim, S. H. Bae, H. J. Chen, N. De Marco and Y. Yang, *Adv. Mater.*, 2016, **28**, 4415–4440.

11 Y. Wang, Y. Lu, W. Ding and D. Mei, *J. Mech. Eng.*, 2020, **56**, 239–252.
12 J. N. Niu, X. Bai, J. W. Wang, Y. Y. Chen, B. Q. Zhao, W. Sha, Y. Long, Z. L. Wang and W. G. Hu, *Adv. Funct. Mater.*, 2024, **35**, 2411916.
13 P. A. Ersman, K. Freitag, M. Nilsson, J. Åhlin, R. Brooke, N. Nordgren, C. Aulin, A. Fall, Y. Nevo and V. Beni, *Adv. Photonics Res.*, 2023, **4**, 2200012.
14 M. Steinberger, A. Distler, J. Hoerber, K. C. Tam, C. J. Brabec and H. J. Egelhaaf, *Flexible Printed Electron.*, 2024, **9**, 025018.
15 A. B. Hamlin, S. A. Agnew, J. C. Bonner, J. W. P. Hsu and W. J. Scheideler, *Nano Lett.*, 2023, **23**, 2544–2550.
16 D. P. Dubal, N. R. Chodankar, D. H. Kim and P. Gomez-Romero, *Chem. Soc. Rev.*, 2018, **47**, 2065–2129.
17 A. Mohapatra, S. K. Tuli, K. Y. Liu, T. Fujiwara, R. W. Hewitt, F. Andrasik, B. I. Morshed and *Ieee, Presented in Part at the 2018 40TH Annual International Conference of the IEEE Engineering in Medicine and Biology Society*, EMBC, 2018.
18 K. I. Nargatti, T. S. Pathak, S. S. Ahankari, J. R. C. Dizon and R. T. Subramaniam, *ACS Appl. Electron. Mater.*, 2023, **6**, 24–46.
19 D. Mitra, K. Y. Mitra, R. Thalheim and R. Zichner, *Phys. Status Solidi A*, 2024, **221**, 2300562.
20 A. J. Kell, K. Wagner, X. Liu, B. H. Lessard and C. Paquet, *ACS Appl. Electron. Mater.*, 2024, **6**, 1–23.
21 Y. Z. N. Htwe, S. Abu Bakar, A. Mohamed, Muqoyyanah, M. H. D. Othman, M. H. Mamat, M. K. Ahmad, M. N. Abd Azis, R. Nuryadi, S. Ramakrishna, N. Salah and A. Alshahrie, *Synth. Met.*, 2024, **306**, 117631.
22 L. Sanchez-Duenas, E. Gomez, M. Larranaga, M. Blanco, A. M. Goitandia, E. Aranzabe and J. L. Vilas-Vilela, *Materials*, 2023, 16.
23 U. Boda, J. Strandberg, J. Eriksson, X. J. Liu, V. Beni and K. Tybrandt, *ACS Appl. Mater. Interfaces*, 2023, **15**, 12372–12382.
24 S. P. Douglas, S. Mrig and C. E. Knapp, *Chem.–Eur. J.*, 2021, **27**, 8062–8081.
25 M. M. Dabour, M. N. Sabry, W. A. Bayoumy and M. A. Mousa, *J. Electron. Mater.*, 2024, **53**, 6221–6227.
26 N. Ibrahim and M. Jaafar, *J. Nanopart. Res.*, 2024, **26**, 17.
27 G. Z. Jia, L. Wu, C. C. He and Y. Li, *IEEE Trans. Plasma Sci.*, 2024, **52**, 5117–5122.
28 S. N. Kholuiskaya, V. Siracusa, G. M. Mukhametova, L. A. Wasserman, V. V. Kovalenko and A. L. Iordanskii, *Polymers*, 2024, **16**(12), 1731.
29 A. J. Kell, K. Wagner, X. Y. Liu, B. H. Lessard and C. Paquet, *ACS Appl. Electron. Mater.*, 2023, **6**, 1–23.
30 L. Zhang, G. Gan, P. Fan, Y. Liu, T. Wang, W. Li and J. Du, *J. Coat. Technol. Res.*, 2023, **20**, 1845–1856.
31 W. Yang, Z. Dong, Z. Guo and C. Wang, *ACS Appl. Electron. Mater.*, 2023, **5**, 2598–2607.
32 Y. Zhou, Z. Xu, H. Bai and C. E. Knapp, *Adv. Mater. Technol.*, 2023, **8**, 2201557.
33 M. Sun, C. Li, Y. Xu, B. Lin, X. Zhang and Y. Sun, *J. Mater. Sci.: Mater. Electron.*, 2024, **35**, 755.
34 Y. Chen, X. Wang, B. Zhang, W. Ma and W. Chen, *J. Mater. Sci.: Mater. Electron.*, 2021, **32**, 22119–22128.
35 S. F. Jahn, T. Blaudeck, R. R. Baumann, A. Jakob, P. Ecorchard, T. Rüffer, H. Lang and P. Schmidt, *Chem. Mater.*, 2010, **22**, 3067–3071.
36 Y. Dong, X. Li, S. Liu, Q. Zhu, M. Zhang, J.-G. Li and X. Sun, *Thin Solid Films*, 2016, **616**, 635–642.
37 R. Ludmerczki, S. Mura, C. M. Carbonaro, I. M. Mandity, M. Carraro, N. Senes, S. Garroni, G. Granozzi, L. Calvillo, S. Marras, L. Malfatti and P. Innocenzi, *Chem.–Eur. J.*, 2019, **25**, 11963–11974.
38 R. Kawabata, T. Matsuda, R. Seo and A. Hirose, *Mater. Lett.*, 2021, **300**, 130205.
39 N. Koga, S. Yamada and T. Kimura, *J. Phys. Chem. C*, 2013, **117**, 326–336.
40 National Center for Biotechnology Information, *PubChem Compound Summary for CID 101599, 1,2,3-Propanetricarboxylic acid, 2-hydroxy-, silver(1+) salt*, vol. **1**, **https://pubchem.ncbi.nlm.nih.gov/compound/Silver-citrate**.
41 National Center for Biotechnology Information, *PubChem Compound Summary for CID 167950, Butanedioic acid, 2,3-dihydroxy-(2R,3R)-, silver(1+) salt*, 2025, vol. **1**, **https://pubchem.ncbi.nlm.nih.gov/compound/167950**.
42 National Center for Biotechnology Information, *PubChem Compound Summary for CID 62364, Silver oxalate*, 2025, **https://pubchem.ncbi.nlm.nih.gov/compound/Silver-oxalate**.
43 National Center for Biotechnology Information, *PubChem Compound Summary for CID 92796, Silver carbonate*, 2025, **https://pubchem.ncbi.nlm.nih.gov/compound/Silver-carbonate**.
44 A. Mazen, *Colloid J.*, 2024, **86**, 138–152.
45 F. Wu, L. Cheng and W. Wang, *Micromachines*, 2022, **13**(4), 638.
46 K. P. Bankura, D. Maity, M. M. R. Mollick, D. Mondal, B. Bhowmick, M. K. Bain, A. Chakraborty, J. Sarkar, K. Acharya and D. Chattopadhyay, *Carbohydr. Polym.*, 2012, **89**, 1159–1165.